

## Structural change of plagioclase glasses by mechanical milling

Yo Shirai<sup>1</sup>, Masayuki Okuno<sup>2\*</sup>, Hiroki Okudera<sup>2</sup>

<sup>1</sup>Kanazawa University, <sup>2</sup>Kanazawa University

Plagioclase( $\text{NaAlSi}_3\text{O}_8$ - $\text{CaAl}_2\text{Si}_2\text{O}_8$ ) melt is important component of magma of the Earth. The information for the structure change of plagioclase glasses by milling is useful to understand earthquake and fault formation and material industry. Silicate glass changes its structure and density even milling as well as heating and compression. For example, it was reported that  $\text{SiO}_2$  glass increase its density with Si-O-Si angle shrinkage and formation of small rings of  $\text{SiO}_4$  tetrahedra<sup>[1]</sup>. In this study, we analyzed the structural changes with milling by X-ray diffraction and FTIR experiments and discussed the composition dependence of milling behaviors of plagioclase glasses.

We synthesized An100 and Ab50An50 composition glasses and milled up to 500 hours by ball mill technique. These milled glasses were analyzed by particle size, X-ray diffraction, and FTIR measurements. By milling about 20-80 hours, apparent average particle size decreases to about 2 micron in diameter. This data also indicate that An100 glass is easy to downsizing than the other glasses. After 20-80 hours, the size re-increased. This indicates the formation of aggregation of small milled glass particles.

The position of First Sharp Diffraction Peak (FSDP) at around  $2\theta=22-26$  deg of XRD pattern related to the size of basic structure unit such as 4 and 6 membered rings of  $\text{TO}_4$  (T=Al/Si) tetrahedra. This peak position shifts to high  $2\theta$  angle with increase of small ring structure of  $\text{TO}_4$  tetrahedra. Obtained results indicate that the structure Ab100 glass change 6 membered ring of  $\text{TO}_4$  dominant to the mixture of 4 and 6 membered ring structure. On the other hand, the shift for An100 glass is small. This may indicate that the structure of non-milled An100 glass has already 4 membered rings dominant structure<sup>[2]</sup>. Previous studies for  $\text{SiO}_2$  glass reported the density increase by milling related with these structure changes<sup>[1]</sup>. The shift of FSDP position of Ab50An50 is larger than the others. Therefore, the structural change of Ab50An50 glass may be larger than the others. The results for FTIR also suggest these results. However, the origin of this variation is complex. A possibility may be formation of the units centered as  $\text{Na}^+$  and  $\text{Ca}^{2+}$  ions.

### References

- [1] Iwao, M and Okuno, M., Koyano, M. and Ktayama, S. (2010) J. Min. Petrol. Sci., Vol. 105, 135-141
- [2] Okuno, M. and Marumo, F. (1982) Mineralogical Journal, Vol.11, 180-196

Keywords: plagioclase glass, ball mill, nano-structure, X-ray diffraction, IR spectroscopy

## X-ray diffraction analysis of pyrope melts at high pressures

Ikumi Yokota<sup>1</sup>, Satoru Urakawa<sup>1\*</sup>, Takumi Kikegawa<sup>2</sup>

<sup>1</sup>Dept Earth Sci, Okayama Univ, <sup>2</sup>KEK PF

Silicate melts play important roles in the chemical evolution of the planetary mantle and crust. Density and viscosity are important physical properties to control the migration of silicate melts, which are strongly related to structure of silicate melts. Thus the structural studies of silicate melts are fundamental to understand magma related processes in the planetary interior. Here we report the results of X-ray diffraction analysis of  $\text{Mg}_3\text{Al}_2\text{Si}_3\text{O}_{12}$  (pyrope) melts at high pressures.

Static structure of pyrope melts has been studied by in situ x-ray diffraction experiments using synchrotron radiation at Photon Factory, KEK, Japan. X-ray diffraction patterns were acquired just above the melting temperature to about 5.5 GPa by energy-dispersive x-ray diffraction method and were analyzed by Fourier method.

The radial distribution functions show the decrease of the peak intensity that is related to the 4-fold coordinated Al-O and Si-O. This is explained by the decrease of the 4-fold coordinated Al and the increase of highly-coordinated Al with pressure. Pyrope includes large amount non-bridging oxygen and high field strength element Mg. Thus Al in the pyrope melt takes highly coordinated state at relatively low pressures.

Keywords: magma, synchrotron radiation, high pressure

## Structure and properties of forsterite-MgSiO<sub>3</sub> liquid interface

Fumiya Noritake<sup>1\*</sup>, Katsuyuki Kawamura<sup>1</sup>

<sup>1</sup>Okayama University

Knowledge about viscosities and permeability of partial molten rocks is important to understand the thermal history of the Earth and volcanism. For understanding those obtained by experiments and estimating the physical properties at extreme conditions that difficult to reproduce in laboratory experiments, knowledge about structure and properties of silicate crystal-liquid interfaces is necessary. In this study, structure and properties of the forsterite-MgSiO<sub>3</sub> liquid interface are investigated by using molecular dynamics simulations. It is essential to know the structure and physical properties of forsterite-MgSiO<sub>3</sub> liquid interfaces since forsterite is the liquidus mineral of primordial magmas.

Molecular dynamics simulations were performed with NPT ensemble using MXDORTO code. The interatomic potential model used in this study is same with used in Noritake et al. (2012). The initial structure is 21440 atom system in which a sheet of MgSiO<sub>3</sub> liquid consist of 8000 atoms is sandwiched between (010) surfaces of forsterite and 43440 atom system in which a sheet of MgSiO<sub>3</sub> liquid consist of 30000 atoms is sandwiched between (010) surfaces of forsterite. Structure and properties in the vicinity of interface was obtained at 0.1 MPa and various temperatures.

From simulation results, characteristic structure was observed in the forsterite-MgSiO<sub>3</sub> liquid interface. In the crystal-liquid interface, 2-30% of SiO<sub>4</sub> tetrahedra of forsterite surface bridge SiO<sub>4</sub> tetrahedra in liquid. In liquid region, SiO<sub>4</sub> tetrahedra concentrate in the vicinity of surface and form an SiO<sub>4</sub> tetrahedra rich layer of 0.4 to 0.6 nm thickness. Inner side of the first SiO<sub>4</sub> rich layer in MgSiO<sub>3</sub> sheet in liquid, the Mg rich second layer of 0.6 nm thickness is formed. Consequently, the structure of liquid is different from that of bulk liquid in 1.2 nm from crystal-liquid surface. However, the biased concentration approaches to bulk composition with the distance from the interface. In the first layer, internal energy of the system is lowered by bridging between SiO<sub>4</sub> tetrahedra at the crystal-liquid interface, and Coulombic interaction between non-bridging oxygen in liquid and magnesium at the crystal surface. In the second layer, interaction between concentrated magnesium and excess oxygen by bridging lower the internal energy.

The 2D self-diffusion coefficient oxygen in the plane in first layer is a half order lower than that of bulk liquid. However, The 2D self-diffusion coefficient of oxygen in Mg-rich second layer is a half order higher than that of bulk liquid. Existence of bridging oxygen between crystal and liquid, and concentration of SiO<sub>4</sub> tetrahedra in first layer might decrease the self-diffusion coefficient of oxygen in the first layer. Concentration of free oxygen, non-bridging oxygen and magnesium might increase the self-diffusion coefficient of oxygen in second layer.

This simulation results suggest that existence of small amount of melt might considerably decrease the viscosities of partial molten rocks and considerably increase permeability of partial molten rocks. However, it should be confirmed that this double layered structure in forsterite-MgSiO<sub>3</sub> liquid interface is equilibrium by performing of long time calculations.

Keywords: Interface, Molecular dynamics simulation, Silicates, Crystal, Liquid

## Chemical heterogeneity in mantle olivine by temperature gradient

Toshinori Yasui<sup>1\*</sup>, Tadashi Kondo<sup>1</sup>

<sup>1</sup>Graduate School of Science, Osaka Univ

Laser-heated diamond anvil cell (LHDAC) has been used as a major method to generate high temperature and pressure conditions of the Earth's interior. In the laser heating experiments, only a local region can be raised to high temperature with a strong temperature gradient in the sample. The Soret effect is known as a phenomenon of chemical diffusion induced by temperature gradient, which causes a change of homogeneous material to heterogeneous chemistry. While the Soret diffusion in liquids has been popularly studied, that in solids and its pressure dependence have not been studied well because the Soret effect is relatively slow and more complex in solids than in liquids. The previous experiments using LHDAC (Heinz & Jeanloz 1987, Sinmyo & Hirose 2010, etc.) reported that a steep temperature gradient makes a large difference of element concentration between the laser-heated spot and its edge, however, the Soret effect in LHDAC have not been quantitatively analyzed.

In this study, we studied the material experienced a steep temperature gradient using LHDAC. Single-crystal or powdered San Carlos olivine with the composition of  $(\text{Mg}_{0.89}\text{Fe}_{0.11})_2\text{SiO}_4$  was used as the starting material. The single-crystal experiments were conducted with NaCl as a pressure medium, while we loaded no pressure medium in powder experiments. Each sample was heated using a Nd:YAG laser without moving laser spot and kept the same temperature gradient. Temperature profile was measured by a spectroradiometric method. The recovered samples were analyzed using Field Emission-Scanning Electron Microscope (FE-SEM) and Electron Probe Microanalysis (EPMA). Experimental pressure and temperature were 10-30GPa and 1000-2000K, heating duration was 10-120 minutes. Various chemical heterogeneity formation was observed in different experimental conditions such as temperature gradient, heating duration and phase transition. We will report the details of these results on the Soret diffusion.

Keywords: LHDAC, Soret effect, diffusion in solid

## Crystal structures of $Zn_2GeO_4$ spinel and $Zn_2SiO_4$ modified spinel phases

Masami Kanzaki<sup>1\*</sup>, Xianyu Xue<sup>1</sup>

<sup>1</sup>Inst. Study Earth's Interior, Okayama U.

High pressure phase relations of  $Zn_2GeO_4$  and  $Zn_2SiO_4$  were studied in 1960s to 1970s (e.g., Syono et al., 1971) in relation to high-pressure mantle minerals, but the crystal structures of high pressure phases discovered have not been determined, except for phase II of  $Zn_2SiO_4$ . In last year's JPGU meeting, we reported the structures of phase III and IV of  $Zn_2SiO_4$  (SIT02-24). Here, we report the crystal structures of cubic and tetragonal spinels in  $Zn_2GeO_4$  and phase V of  $Zn_2SiO_4$ , and also present new structural insights regarding phase III and IV of  $Zn_2SiO_4$ .

All samples were synthesized using 5000ton Kawai-type multianvil press at Misasa. Starting materials were  $Zn_2GeO_4$  and  $Zn_2SiO_4$  phenacite phases synthesized at ambient pressure. Powder X-ray diffraction patterns were obtained at BL19B2 of SPring-8 using a large Debye-Scherrer camera. For refinement, the Rietveld method was used (RIETAN-FP). Details of the procedure are same as those of Kanzaki and Xue (2012). <sup>29</sup>Si MAS NMR spectrum of phase V was also obtained.

Cubic and tetragonal spinels of  $Zn_2GeO_4$  were synthesized at 3 GPa and 1600 °C, and 5 GPa and 1200 °C, respectively. As expected, these spinels have inverse-type in which the tetrahedral site is occupied by Zn. For tetragonal spinel, the symmetry is lowered as a result of ordering of Zn and Ge in the octahedral sites. The tetragonal spinel phase is isostructural to  $Zn_2TiO_4$ . Bond distances calculated by Brown's bond valence agree well with the experimental values from the present study.

For the structures of phase III and IV of  $Zn_2SiO_4$ , after last year's presentation (SIT02-24), we noted that phase III is isostructural to the high-temperature phase of  $(Zn_{1.1}Li_{0.6}Si_{0.3})SiO_4$  (Liu et al., 2013). The latter structure is related to the olivine structure in that metal cations occupy vacant tetrahedral sites, rather than octahedral sites of the olivine structure, and is referred to as "tetrahedral olivine" by Baur (1980). In phase IV, triclusters made of two  $ZnO_4$  and one  $SiO_4$  sharing a common oxygen form columns running along the c-direction. Similar columns also exist in phase II, which explains the similar densities of phases II and IV.

We refined crystal structure of phase V of  $Zn_2SiO_4$ , and confirmed that it has a modified spinel structure. Its structural parameters are similar to those of  $Mg_2SiO_4$  wadsleyite. Octahedral sites are occupied by Zn only, and no Zn/Si disorder was detected. This is consistent with the <sup>29</sup>Si MAS NMR result that revealed a single peak of tetrahedral Si for phase V.

Baur, W.H., *Inorg. Nucl. Chem. Lett.*, 16, 525-527, 1980

Kanzaki, M. and Xue, X., *Inorg. Chem.*, 51, 6164-6172, 2012

Liu, X., Kanzaki, M and Xue, X, *Phys. Chem. Mineral.*, submitted

Syono, Y., Akimoto, S., and Matsui, Y., *J. Solid State Chem.*, 3, 369-380, 1971

Keywords:  $Zn_2SiO_4$ ,  $Zn_2GeO_4$ , high pressure phase, crystal structure, spinel, crystal chemistry

## High-Pressure Transitions of NaZnF<sub>3</sub> and NaMnF<sub>3</sub> Perovskites with Implication to MgSiO<sub>3</sub> Postperovskite Analogues

Masaki Akaogi<sup>1\*</sup>, SHIRAKO, Yuichi<sup>1</sup>, NAGAKARI, Takayuki<sup>1</sup>, KOJITANI, Hiroshi<sup>1</sup>, YUSA, Hitoshi<sup>2</sup>, YAMAURA, Kazunari<sup>2</sup>

<sup>1</sup>Dept. Chem., Gakushuin University, <sup>2</sup>Nat. Inst. Mater. Sci.

It is accepted that MgSiO<sub>3</sub>-rich perovskite (Pv) transforms to postperovskite (pPv) in the lowermost mantle. Investigations on MgSiO<sub>3</sub> pPv properties are of great interest to clarify the structure and dynamics of the core-mantle boundary region. However, because of high stability pressure and temperature of MgSiO<sub>3</sub> pPv exceeding 120 GPa and 2000 oC and amorphization of the pPv on release of pressure, ABX<sub>3</sub> compounds that undergo the Pv-pPv transition at lower pressure and are quenchable to ambient conditions are important as analogues for MgSiO<sub>3</sub>. In recent years, we found that CaRuO<sub>3</sub>, CaRhO<sub>3</sub>, NaNiF<sub>3</sub> and NaCoF<sub>3</sub> undergo the Pv-pPv transition below about 20 GPa, and determined the phase relations. We also refined the pPv structures and measured some physical properties (Kojitani et al., 2007, Shirako et al., 2009, 2012, Yusa et al., 2012). In this study, we have examined high pressure transitions in NaZnF<sub>3</sub> and NaMnF<sub>3</sub> and determined the phase relations as well as structural refinement of the NaZnF<sub>3</sub> pPv. Combining the previous results on NaNiF<sub>3</sub> and NaCoF<sub>3</sub>, we discuss on A+B<sub>2</sub>+F<sub>3</sub> fluorides as analogue compounds for the Pv-pPv transition in MgSiO<sub>3</sub>.

High pressure experiments on NaZnF<sub>3</sub> and NaMnF<sub>3</sub> were made at 9-24 GPa and 600-1000 oC using a multianvil apparatus. The recovered NaZnF<sub>3</sub> samples were crushed into powder in liquid nitrogen, and examined by powder X-ray diffraction for phase identification. The run products of sintered NaMnF<sub>3</sub> samples were examined by microfocus X-ray diffraction method. The structure of NaZnF<sub>3</sub> pPv was refined by Rietveld analysis.

NaZnF<sub>3</sub> Pv transforms to pPv at 10-15 GPa. The NaZnF<sub>3</sub> pPv partially transforms back to Pv on release of pressure. The transition boundary in NaZnF<sub>3</sub> is expressed as  $P(\text{GPa}) = 4.9 + 0.011T(\text{oC})$ , and its volume change is -1.9 %. At 8-11 GPa, NaMnF<sub>3</sub> Pv dissociates into two phases of Na<sub>3</sub>Mn<sub>2</sub>F<sub>7</sub> and MnF<sub>2</sub>. Although the MnF<sub>2</sub> phase in the recovered samples has a ?PbO<sub>2</sub>-type structure, it is suggested to be an O-I type or cotunnite-type structure at high pressure. The refined structure of NaZnF<sub>3</sub> pPv is close to that of NaNiF<sub>3</sub> pPv. Deformation of octahedra in the two pPv structures is similar to that of MgSiO<sub>3</sub> pPv at 120 GPa (Murakami et al., 2004), but is smaller than those in CaMO<sub>3</sub> pPv (M = platinum group elements and Sn). The Pv-pPv transitions in NaZnF<sub>3</sub>, NaNiF<sub>3</sub> and NaCoF<sub>3</sub> occur at pressure below about 20 GPa. The axial compressibilities of Pvs and pPvs of the three fluorides change in the same order as those of MgSiO<sub>3</sub> Pv and pPv. The Pv-pPv transitions in the three fluorides occur at the Pv octahedral tilt-angle of about 26o, at which the transition occurs in MgSiO<sub>3</sub>. All of the above results suggest that the fluorides are good quenchable, low-pressure analogues for the Pv-pPv transition in MgSiO<sub>3</sub>. In particular, NaNiF<sub>3</sub> is most valuable, because the pPv phase is quenchable as the single-phase material at ambient conditions.

Keywords: perovskite, postperovskite, high-pressure transition, fluoride, lower mantle, analogue material

## Ab initio computation on the Fe L-edge X-ray emission spectroscopy of Fe-bearing Mg-SiO<sub>3</sub>

Xianlong Wang<sup>1\*</sup>, Taku Tsuchiya<sup>1</sup>

<sup>1</sup>Geodynamics Research Center, Ehime University

Behaviors of iron (Fe) in the minerals of the Earth's lower mantle (LM), including valence state, spin state, and chemical environments, at high pressures are important for more detailed understanding the LM properties. The pressure induced spin transition of Fe-bearing MgO and MgSiO<sub>3</sub> perovskite (Pv) were detected of usually by using high-resolution *K*-edge X-ray emission spectroscopy (XES) [1,2,3] and confirmed by theoretical simulations [4,5]. Since the Fe *K*-edge XES is associated to the 3*p* orbital, which is far from the valence orbitals (3*d* and 4*s*), it provides no information about Fe's coordination environments. However, Fe *L*-edge XES can directly determine the distribution and intensity of Fe-3*d* character. To identify the spin state, valence state and substitution site of Fe in Fe-bearing Pv at the LM pressure range, we systematically investigated the *L*-edge XES of Fe<sup>2+</sup>- and Fe<sup>3+</sup> (Al<sup>3+</sup>)-bearing Pv under high pressure by using the first-principles method combined with the Slater-transition method. Our results show that the spin transition of Fe<sup>2+</sup> and Fe<sup>3+</sup> can be identified easily by the *L*-edge XES technique. The valence state of Fe can be furthermore certified, since the shift of the first main peak of Fe<sup>3+</sup> is about two times larger than that of Fe<sup>2+</sup> across the spin transition. The width of the *L*-edge XES of Fe<sup>3+</sup> is also sensitive to the substitution site, indicating that their coordination environments might also be distinguishable from the Fe *L*-edge XES spectra. These strong sensitivities to the Fe states suggest that the high-resolution Fe *L*-edge XES measurement would be a useful experimental technique to investigate Fe-bearing silicate minerals. Corresponding experiments are expected.

Keywords: First-principles calculation, First-principles calculation, Fe L-edge XES, Mg perovskite

## Synchrotron XRD and Mossbauer spectroscopic study on $\text{Ca}_2\text{MgSi}_2\text{O}_7$ - $\text{Ca}_2\text{Fe}^{3+}$ series melilite at high pressures

Maki Hamada<sup>1\*</sup>, Eiji Ohtani<sup>1</sup>, Takaya Mitsui<sup>2</sup>, Ryo Masuda<sup>2</sup>, Masahide Akasaka<sup>3</sup>

<sup>1</sup>Tohoku Univ., <sup>2</sup>JAEA, <sup>3</sup>Shimane Univ.

Synthetic  $\text{Ca}_2\text{MgSi}_2\text{O}_7$  (akermanite: Ak)- $\text{Ca}_2\text{Fe}^{3+}\text{AlSiO}_7$  (ferrialuminium gehlenite: FAGeh) series melilites were investigated using synchrotron X-ray diffraction and synchrotron-radiation-based Mossbauer spectroscopic methods to determine the distribution of  $\text{Fe}^{3+}$  between two structurally independent tetrahedral sites (T1 and T2), and the relationship between ionic substitution and incommensurate structure in melilite at high pressures.  $^{57}\text{Fe}$ -doped Ak-FAGeh melilites were synthesized from starting material with composition of  $\text{Ak}_{50}\text{FAGeh}_{50}$  by sintering technique at 1140-1180 °C and 1 atm for high pressure experiment. The average chemical composition of the synthetic melilites was  $\text{Ca}_{2.00}\text{Mg}_{0.56}\text{Fe}^{3+}_{0.42}\text{Al}_{0.44}\text{Si}_{1.57}\text{O}_7$ . The site populations at the T1 and T2 sites at the synthetic condition were determined by X-ray Rietveld analysis and  $^{57}\text{Fe}$  Mossbauer spectroscopy (340MBq  $^{57}\text{Co}$  source) to be  $[0.557\text{Mg}+0.280\text{Fe}^{3+}+0.237\text{Al}]_{\text{T1}}$   $[0.197\text{Fe}^{3+}+0.176\text{Al}+1.574\text{Si}]_{\text{T2}}$  (apfu: atoms per formula unit), which is consistent with that by Hamada and Akasaka (in press).

The experiments at high pressures were performed using a diamond anvil cell (DAC) with culet size of 0.3 mm. A Rhenium gasket was pre-indented to 0.06 mm in thickness, and a hole with 0.1 mm in a diameter was drilled in the gasket as the sample chamber. NaCl was used as pressure medium. In addition to the powder sample, several ruby tips (0.01-0.02 mm in diameter) were put into the chamber as a pressure marker. The pressure was estimated based on Ruby fluorescence (Mao et al., 1978). Mossbauer spectra and X-ray diffraction were taken at the beamline BL11XU of SPring-8. The energy of used gamma-ray for Mossbauer spectroscopy was 14.4125 keV. Mossbauer spectra were measured at 0.8, 1.6, 14.1, 18.7 GPa. The spectra were fitted to Lorentzians with widths and intensities constrained to be equal at each site, using synchrotron-based-Mossbauer analysis program S8QBMOSS (Hamada and Akasaka, in prep.).

At 0.8 and 1.6 GPa, Mossbauer spectra consisted of two doublets assigned to T1 and T2 sites. However, Isomer Shifts (*I.S.*) of T1 and T2 sites at 1.6 GPa (0.11(5) and 0.05(5) mm/s, respectively) were smaller than those at ambient condition. Area ratio of  $\text{Fe}^{3+}(\text{T1}):\text{Fe}^{3+}(\text{T2})$  at ambient condition was 47(1):53(2) (Hamada and Akasaka, in press). Whereas, area ratio at 0.8 and 1.6 GPa were 52(10):48(9) and 44(9):56(8), respectively. Mossbauer spectra at 14.1 and 18.7 GPa consisted of only one doublet assigned to  $\text{Fe}^{3+}$  at T2 site. However, the half width was broad, suggesting that the spectrum consists of strongly superimposed doublets.

The variation of the Mossbauer hyperfine parameters (*I.S.* and quadrupole splitting *Q.S.*) suggests that covalencies of T1-O and T2-O bonds increase and difference of geometric properties (site distortion and mean T-O distance) between  $\text{T1O}_4$  and  $\text{T2O}_4$  tetrahedra becomes smaller with increasing pressure. Yang et al. (1997) reported the incommensurate (IC)-normal (N) phase transition at 1.7 GPa. The smaller *I.S.* values may be caused by IC-N phase transition.

Keywords: Synchrotron X-ray diffraction, Synchrotron Mossbauer spectroscopy, Synthetic melilite, Incommensurate structure, High pressure

## Magnetic phase diagram of (Mg,Fe)O: reinvestigation

Atsuhiko Fujii<sup>1\*</sup>, Tadashi Kondo<sup>1</sup>, Toshifumi Taniguchi<sup>1</sup>

<sup>1</sup>Graduate School of Science, Osaka Univ.

(Mg,Fe)O shows complex magnetic behavior due to the presence of non-magnetic magnesium ion. For example,  $(\text{Mg}_{0.23}\text{Fe}_{0.77})_{0.92}\text{O}$  shows Neel transition at 128 K and spin-glass like phenomena below 76 K at ambient pressure [Abbas and Hicks, 1990]. Although we reported a magnetic phase diagram and suggested that the magnetic structure would be differ between iron-rich side and magnesium-rich side [Fujii et al. 2011], the magnetic property of (Mg,Fe)O at ambient pressure is still unclear. In this study, we reexamined the compositional dependence of magnetic ordering of (Mg,Fe)O at ambient pressure. We used Superconducting Quantum Interference Device (SQUID) magnetometer (MPMS-7 or MPMS-XL, Quantum design Inc.) to measure the temperature dependence of magnetic susceptibility by cooling sample in zero field (ZFC) and in a field (FC). The magnetic field dependent of susceptibility and the temperature dependence of AC magnetic susceptibility were newly measured. In the iron-rich (Mg,Fe)O, the ZFC curve show a peak-like cusp at relatively high temperature and a kink at low temperature. An irreversibility was observed between the ZFC curve and FC curve below the kink temperature. These behaviors are the same as those of  $(\text{Mg}_{0.23}\text{Fe}_{0.77})_{0.92}\text{O}$  observed in the previous study [Abbas and Hicks, 1990]. Therefore, the kink and the cusp would indicate a spin-glass transition and Neel transition, respectively. In the case of the magnesium-rich (Mg,Fe)O, the ZFC curve show no kink and an irreversibility below the cusp temperature. Therefore, it would show no Neel transition but spin-glass transition. We also observed a superparamagnetic like phenomena in all sample. These interpretations are supported by the magnetic field dependence of susceptibility and the AC magnetic susceptibility measurement. Therefore, the magnetic ordering of magnesium-rich (Mg,Fe)O is distinctly different from iron-rich (Mg,Fe)O at ambient pressure.

Keywords: (Mg,Fe)O, magnetic ordering

## Temperature quenching mechanism of cathodoluminescence in forsterite

Hirotsugu Nishido<sup>1\*</sup>, Taro Endo<sup>1</sup>, Kiyotaka Ninagawa<sup>1</sup>, Masahiro Kayama<sup>2</sup>, Arnold Gucsik<sup>3</sup>

<sup>1</sup>Okayama University of Science, <sup>2</sup>Hiroshima University, <sup>3</sup>Tohoku University

Recently, cathodoluminescence (CL) zoning of the forsterite in carbonaceous meteorites has been investigated to clarify the origin and thermal history of the chondrules. CL spectroscopy can detect a trace amount of impurity elements such as Mn, Cr and Ti and lattice defects, which relate to Al-O centers and primary intrinsic centers. However, a small amount of divalent Fe ions as quencher easily eliminate CL emissions caused by any luminescent centers, so only near end forsterite could emit CL. In this study CL spectroscopy of forsterite samples has been conducted to interpret emission mechanism of their luminescent centers by an SEM-CL, and quantitatively analyze a thermal effect on forsterite CL by assuming the Mott-Seitz quenching model.

Forsterite crystals (Fo: 99.1) in basalt from Mogok, Myanmar and micro-grains (Fo: 99.7-99.8) in chondrules from Allende and Kaba meteorites classified as a CV3 were prepared for CL spectral measurements. CL spectroscopy was made by a SEM-CL system, which is comprised of SEM (JEOL: JSM-5410) combined with a grating monochromator (OXFORD: Mono CL2) at accelerating voltage of 15 kV and beam current of 1.0 nA in a beam scan mode. The sample temperature was controlled by flowing liquid nitrogen and using an embedded heater in a cryostage. All spectra were corrected for total instrumental response, which was determined using a calibrated standard lamp.

At room temperature, the CL spectra show broad emission bands at around 400 nm in blue region and at around 650 nm in red region, and pronounced emissions increasing to IR region with small emissions at around 720 nm. These bands can be assigned to structural defect, divalent Mn and trivalent Cr impurities, respectively. Their emission intensities increase with a decrease in sample temperature. In general, luminescence efficiency decreases with rising temperature due to an increase in non-radiative transitions, which has been known as temperature quenching.

CL spectral peaks in energy unit were deconvoluted by Gaussian curve fitting to determine the emission component for each emission center. The emission peak in blue region can be separated into two components centered at 3.15 and 2.99 eV, and the peaks caused by Mn and Cr impurity centers can be fixed at 1.91 and 1.74 eV, respectively. By assuming the Mott-Seitz model, activation energy in each temperature quenching process can be calculated by Arrhenius plots using integral intensity of each component. The straight-line relationships in the plots resulted in each activation energy as follows; blue emission at 3.15 eV: 0.08-0.04 eV, blue emission at 2.99 eV: 0.10-0.05 eV, red emission at 1.91 eV: 0.01-0.005 eV, red emission at 1.74 eV: 0.01-0.02 eV. The values of activation energies for blue emissions caused by structural defects correspond to the vibration energy of Si-O stretching mode in the lattice, and the values for red emissions caused by Mn and Cr impurity centers to Mg-O vibration energy. It suggests that the temperature quenching energy might be transferred as a phonon to the specific lattice vibration.

Keywords: forsterite, cathodoluminescence, temperature quenching

## Measurements of elastic constants of single-crystal chromian spinel by frequency resonant ultrasound spectroscopy

Kenya Ono<sup>1\*</sup>, Yuya Harada<sup>2</sup>, Akira Yoneda<sup>3</sup>, Junji Yamamoto<sup>4</sup>, Tohru Watanabe<sup>1</sup>

<sup>1</sup>Department of Earth Sciences, University of Toyama, <sup>2</sup>Department of Earth and Planetary Systems Science, Faculty of Science, Hiroshima University, <sup>3</sup>Institute for Study of the Earth's Interior, Okayama University, <sup>4</sup>Hokkaido University Museum, Hokkaido University

Chromian spinel grains in mantle xenoliths usually contain fluid inclusions whose residual pressure (fluid density) can provide us the origin depth of the xenoliths. Elastic properties of chromian spinel are essential for precise estimation of the origin depth. Although elastic constants of spinel ( $\text{MgAl}_2\text{O}_4$ ) and chromite ( $\text{FeCr}_2\text{O}_4$ ) have been already reported, few studies have been done on chromian spinel. We thus have studied elastic constants of a chromian spinel single-crystal via a resonance method.

Chromian spinel grains were collected from mantle xenoliths from Sveyagin, Russia (Yamamoto et al., 2009, Island Arc). One grain was selected in terms of the uniformity of crystallographic orientation examined by SEM-EBSD. The selected grain was shaped into a rectangular parallelepiped ( $0.517 \times 0.417 \times 0.412 \text{ mm}^3$ ). Each face was polished flat ( $< 1$  micrometer) in an orientation perpendicular to  $\{100\}$  or  $\{110\}$ . The crystallographic orientation of the specimen was determined by the X-ray precession method. The density is  $3.83(1) \times 10^3 \text{ kg/m}^3$ , which is calculated from the chemical composition analyzed with EPMA and the lattice parameter ( $a = 0.8115(1) \text{ nm}$ ) determined by XRD.

Lower 16 oscillation modes were observed in the frequency range from 4 to 9 MHz. The oscillation of a specimen is not free oscillation, because the specimen is held between two transducers. A specimen-holding force  $F$  affects resonance frequencies. In order to infer the resonance frequencies of free oscillation, resonance frequencies were measured as a function of the specimen-holding force  $F$  and then extrapolated to  $F=0$ .

Elastic constants are determined by comparing calculated and measured resonance frequencies. FEM was employed to calculate resonance frequencies.  $C_{11}$ ,  $C_{12}$  and  $C_{44}$  are 264(3), 154(3), and 142.6(2) (GPa), respectively. Compared with elastic constants of end members, spinel (Yoneda, 1990) and chromite (Hearmon, 1990), chromian spinel has the lowest  $C_{11}$  and intermediate  $C_{12}$  and  $C_{44}$ .

Keywords: elastic constants, chromian spinel, resonance method, mantle xenoliths

## Three dimensional visualization of residual pressure around inclusions in sapphire

Hiroyuki Kagi<sup>1\*</sup>, Nanako Kamegata<sup>1</sup>, Jocelyn Fuetes<sup>1</sup>, Naoki Noguchi<sup>1</sup>, Ahmadjan Abduriyim<sup>2</sup>

<sup>1</sup>Graduate School of Science, University of Tokyo, <sup>2</sup>Gemological Institute of America

Mantle derived minerals can tell us much information about processes within the deep Earth. It is important to determine the original depth of these mineral samples. Kagi et al. 2009 showed that three-dimensional Raman mapping observations can be used to visualize the distribution of residual pressure around inclusions in diamond, which has provided information about the depth of diamond formation. Corundum is the second hardest mineral after diamond and is expected to also show substantial residual pressure around inclusions.

Samples were collected from New South Wales, Australia as well as Chanaburi, Thailand and are associated with alkali basalts. It is possible to distinguish between corundum crystals formed from various settings, such as metamorphic versus igneous settings, based on trace element analyses. However, distinguishing between crystals of different geographic locality and similar geologic settings is not yet possible using nondestructive methods. Based on current geochemical observations, there are two models for the formation of igneous corundum crystals. Guo et al. 1996 proposed that these crystals formed in the middle crust by a hybrid reaction between carbonatite melt and silicic magma. Alternatively, Sutherland et al. 1998 suggested that they may form directly from volatile-rich felsic melts generated at lower crustal conditions. By using 3D mapping techniques, it may be possible to evaluate the P-T history of the host rock as well as differentiate between gems from different localities.

The fluorescence spectrum of corundum has two peaks associated with the excitation of Cr<sup>3+</sup> impurities in its structure, R1 and R2. Because the R2 line is insensitive to differential stress, the residual pressure can be calculated based on the peak shift of the R2 line using a pressure calibration curve.

The samples were excited using 514.5 nm emission of Ar-ion laser with a diameter of 2 micron. Measurements were taken every 5 to 10 micrometers around albite, zircon, and rutile inclusions using a point-by-point mapping illumination system. The R2 and R1 lines of the fluorescence spectra were fitted by Lorentzian functions after subtraction of background. In order to account for peak oscillations caused by changes in room temperature, real-time calibration of the fluorescence spectra energy axes were performed by neon emission lines as discussed in Odake et al. 2008.

Over 25 two- and three-dimensional maps of various inclusions have been created so far. The maximum residual pressure for each map ranges from 0.1 GPa to 0.51 GPa. In many of these samples, stress distribution can be explained by differences in elastic constants between the host and inclusion. For example, our results show one slice of a 3D map around a zircon inclusion. In this case, the c-axis of the corundum and the c-axis of the zircon are nearly parallel. With decreasing temperature and pressure, the c-axis is expected to have higher residual pressure due to differences in linear thermal expansion coefficients and bulk moduli between the host and inclusion. It is clear that the c-axis has the highest residual pressure, as expected. Another notable observation is that the maximum residual pressure surrounding zircons correlates with length of the crystal along the c-axis. Two distinct trends between residual pressure and length are observed. This may be due to many factors including the relative orientation of the host and inclusion or the presence of cracks surrounding the inclusion. It could also be due to the different geographic localities. However, more measurements need to be taken to confirm.

Previous methods to determine original depth, such as those used by Barron 2005 and Izraeli et al. 1999, which assume isotropic elastic properties in inclusion and diamond, cannot be used in these corundum-inclusion pairs. Our results show that relative orientation of corundum and inclusions must be accounted for in future calculations of P-T history.

Keywords: residual pressure, fluorescence spectra, ruby, sapphire, inclusions

## Ab initio quantum chemical investigation of arsenic sulfide molecular diversity

Atsushi Kyono<sup>1\*</sup>

<sup>1</sup>Div. of Earth Evolution Sci., Grad. Sch. of Life & Environmental Sci., Univ. of Tsukuba

The structural diversity of arsenic sulfide molecules in compositions between  $As_4S_6$  and  $As_4S$  was investigated using ab initio quantum chemical calculations. The  $As_4S_6$  molecule consists of four trigonal pyramidal coordinations of As atoms bonding to three S atoms. In the  $As_4S_5$  composition, only one type of molecular configuration corresponds to an uzonite-type molecule. In the  $As_4S_4$  composition, two molecular configurations exist with realgar-type and pararealgar-type molecules. Three molecular configurations are in the  $As_4S_3$  composition. The first configuration comprises trigonal pyramidal As atom coordinations of two types: bonding to two S atoms and one As atom, and bonding to one S atom and two As atoms. The second is the molecular configuration of dimorphite. The third comprises trigonal pyramidal As atom coordinations of two types: bonding to three As atoms, and bonding to one As atom and two S atoms. The  $As_4S_2$  composition allows molecular configurations of two types. One is comprised of trigonal pyramidal As atom configurations of one type bonding to two As atoms and one S atom. The other comprises trigonal pyramidal As atom coordinations of three types: bonding to two S atoms and one As atom, bonding to one S atom and two As atoms, and bonding to three As atoms. The  $As_4S$  molecule has trigonal pyramidal As atom coordinations of two types: bonding one S atom and two As atoms, and bonding to three As atoms. The  $As_4S$  composition permits only one molecular configuration, which suggests that the mineral duranusite comprises the  $As_4S$  molecular geometry. In all, ten molecular configurations are predicted in the molecular hierarchy of the arsenic sulfide binary system. The simulated Raman spectral profiles are helpful in searching for undiscovered arsenic sulfide minerals.

Keywords: arsenic sulfide minerals, molecular configuration, diversity, hierarchy, ab initio quantum chemical calculation

## Volume and crystal structure change due to He incorporation into cristobalite at high pressures

Masanori Matsui<sup>1\*</sup>, Tomoko Sato<sup>2</sup>, Nobumasa Funamori<sup>3</sup>

<sup>1</sup>School of Sci., Univ. of Hyogo, <sup>2</sup>Dept. of Earth and Planetary Systems Sci., Hiroshima Univ., <sup>3</sup>Dept. of Earth and Planetary Sci., Univ. of Tokyo

Based on powder X-ray diffraction measurements under high pressures and room temperature at Photon Factory, Tsukuba, Sato et al.(2012) have recently found unique behavior of cristobalite in helium pressure medium in a diamond anvil cell, where, on compression, cristobalite II transforms to a new phase (called cristobalite-He I) at about 8 GPa, then on subsequent decompression from about 15 GPa, cristobalite-He I transforms to another new phase (called cristobalite-He II) at about 7 GPa. They tentatively assigned cristobalite-He I and II to have orthorhombic and rhombohedral lattices with molar volumes greater than about 30 % and 25 % larger than cristobalite, respectively. Here we use first-principle calculations to study structural and energetic properties of cristobalite-He I and II in more detail.

All calculations were performed with the ab initio simulation package VASP (Kresse and Furthmuller, 1996). The projector-augmented wave (PAW) method (Blochl, 1994) was used in the generalized-gradient approximation (GGA) for the exchange-correlation functional (Perdew et al., 1996). Atomic positions were relaxed with observed or hypothetical crystal-symmetry constraints. In order to check the reliability and applicability of the computations, we first calculated the structures and energies of cristobalite and cristobalite II, with the results that the calculated values reproduce the observed ones (Dove et al., 2000; Dera et al., 2011) accurately.

Cristobalite transforms to cristobalite II at 1.5 GPa and room temperature (Palmer and Finger, 1994; Dove et al., 2000). The initial lattice parameters and atomic positions of both Si and O were taken from cristobalite II (Dove et al., 2000; Dera et al., 2011), while the He positions were taken to be situated in large voids in cristobalite II. We tested several structural models for both cristobalite-He I and II, and finally found enthalpy-minimized models that reproduces the measured X-ray diffraction patterns of the two phases (Sato et al., 2011), respectively, accurately.

Keywords: cristobalite, helium, high pressure, crystal structure, phase transition

## Stability of Orthopyroxene in pyroxene quadrilateral at 1 atm and High Temperatures

Shugo Ohi<sup>1\*</sup>

<sup>1</sup>Graduate School of Science, Kyoto University

Pyroxene is one of the most important rock-forming minerals not only for its abundant occurrence but also for various paragenesis which provide information on the thermal history of pyroxene-bearing rocks. In the system  $Mg_2Si_2O_6$  (En) -  $CaMgSi_2O_6$  (Di), there had been the controversy about the appearance and stability of the orthopyroxene (Opx) phase near 1400 C other than protopyroxene (Ppx) since the discovery by Foster and Lin (1975). In recent years, Ohi et al. (2008) observed the phase transition between low-temperature Opx (LT-Opx) and high-temperature Opx (HT-Opx) at 1170 C during both heating and cooling processes by high-temperature synchrotron X-ray powder diffraction experiments for the composition of  $(Ca_{0.06}Mg_{1.94})Si_2O_6$ . They concluded that Opx the phase near 1400 C was HT-Opx and that below 1000 C was LT-Opx. In  $Mg_2Si_2O_6$ - $CaMgSi_2O_6$ - $CaFeSi_2O_6$ - $Fe_2Si_2O_6$  system, Opx contain a little amount of Ca and have the composition between  $Mg_2Si_2O_6$ - $Fe_2Si_2O_6$  solid solution. However, there was no report about the stability field of HT-Opx in pyroxene quadrilateral system. Purpose in present study is to reveal the stability field of LT- and HT-Opx in pyroxene quadrilateral system by synthesis experiments.

About 20 samples were synthesized from gels with 6 kinds of composition in the range of Ca : Mg : Fe = 0.03-0.15 : 0.92-0.65 : 0.05-0.20 at 1180, 1280, 1345 and 1375 C. Run durations were about 3-14 days. All samples were synthesized dry at 1 atm using a  $H_2 + CO_2$  gas mixture to maintain the oxygen fugacity near that of the iron-wüstite assemblage. They were analyzed with X-ray powder diffractometer (XRD: RIGAKU, SmartLab), a scanning electron microscope (SEM: HITACHI S-3000H) + energy dispersive X-ray spectrometer (EDX: HORIBA EMAX7000) and an electron backscattered diffraction (EBSD: HKL, CHANNEL5). Peaks of clinopyroxene (Cpx: inverted from protoenstatite) and pigeonite (Pig) were not identified by XRD in present study. Therefore, these phases were described as Ca-poor Cpx.

At 1180 C, most crystals were smaller than 5  $\mu m$  in diameter and the chemical compositions of those could not be analyzed method by SEM-EDX. All XRD patterns of crystals synthesized at 1180 C showed the presence of Ca-poor Cpx and (or) Di and there were no Opx peaks in XRD spectra. At 1280 C, most crystals were about 3-5  $\mu m$  in diameter and some crystals were large enough to be analyzed by SEM-EDX. Analytical data by SEM-EDX showed the presence of Opx ( $Ca_{0.06}Mg_{1.84}Fe_{0.10}Si_2O_6$ ). XRD patterns showed the presence of Opx in the samples with chemical compositions of  $Fs/(En + Fs) > 0.1$ , whereas there were no Opx in the sample  $Fs/(En + Fs) < 0.1$ . At 1345 and 1375 C, most crystals were about 5-10  $\mu m$  in diameter. Analytical data by SEM-EDX and SEM-EBSD showed the presence of Cpx, Opx, Pig and Di.

In Fe-free En-Di system at 1 atm, the stability field of LT-Opx is below 1005 C and that of HT-Opx is above 1370 C. In present study, there were Opx in some samples synthesized above 1280 C whereas there were no Opx in samples synthesized at 1180 C. It suggested that all Opx in present study were HT-Opx and the stability field of HT-Opx was spread to lower temperature with increasing Fe-content in HT-Opx. This trend was same as the stability field of Pig.

Keywords: orthopyroxene, high temperature, enstatite-diopside-hedenbergite-ferrosilite system, phase transition

## Thermal equation of state of manganite

Akio Suzuki<sup>1\*</sup>

<sup>1</sup>Tohoku University

Manganese(III) oxide hydroxide is found in nature as the minerals groutite (alpha-MnOOH), feitknechtite (beta-MnOOH), and manganite (gamma-MnOOH). Manganite is one of the naturally occurring polymorphs of Mn<sup>3+</sup>-OOH with an InOOH-related structure. The oxide hydroxides of trivalent cations have an InOOH-related structure, in which the trivalent cation is octahedrally coordinated by oxygen. InOOH, beta-CrOOH, epsilon-FeOOH, and delta-AlOOH have orthorhombic unit cells. However, manganite is monoclinic because of the Jahn-Teller distortion. Here we report the pressure-volume-temperature relation of gamma-MnOOH. The aim of this study was to determine the compression behavior of an oxide hydroxide with an InOOH-related structure.

The high-pressure X-ray diffraction study was carried out at the station NE7A at the Photon Factory Advanced Ring (PF-AR) in High Energy Acceleration Research Organization (KEK). The PF-AR operates at 6.5 GeV with an injection current of 60 mA. We used a Kawai-type multianvil apparatus driven by a large volume press, MAX-III. Tungsten carbide cubes (Tungaloy grade F) of 22 mm edge length were used for high-pressure generation.

Experiments were performed up to a pressure of 18.0 GPa and a temperature of 700K. The pressure-volume data were fitted by a third-order Birch-Murnaghan equation of state with the following parameters:  $V_0 = 135.22(8) \text{ \AA}^3$ ,  $K_0 = 77(2) \text{ GPa}$  and  $K_{0T} = 12.0(5)$ . The temperature dependence of the bulk modulus was determined to be  $dK/dT = -0.022(6) \text{ GPa/K}$ . This study shows that the most compressible axis is the b-axis. The beta angle in the monoclinic unit cell decreases with increasing pressure.

Keywords: X-ray diffraction, Equation of state, High pressure, MnOOH, Synchrotron radiation, Hydrous mineral

## Thermal expansivities of stishovite and akimotoite by high-pressure Raman and high-temperature X-ray diffraction methods

Monami Yamazaki<sup>1\*</sup>, Hiroshi Kojitani<sup>1</sup>, Masaki Akaogi<sup>1</sup>

<sup>1</sup>Dept. Chemistry, Gakushuin Univ

High-pressure high-temperature experiments suggest that SiO<sub>2</sub> stishovite and MgSiO<sub>3</sub> akimotoite are constituents of subducted oceanic plate and continental crust. Because they are unstable at 1 atm and at high temperatures, it is difficult to directly measure their thermal expansivities. Therefore, they have been poorly constrained. In this study, we have determined thermal expansivities of SiO<sub>2</sub> stishovite and MgSiO<sub>3</sub> akimotoite by theoretical calculation based on high-pressure Raman spectroscopic data and high-temperature X-ray diffraction measurements.

High-pressure Raman spectroscopy was performed in a pressure range from 1 atm to 10 GPa using a diamond anvil cell and a micro-Raman spectrometer. SiO<sub>2</sub> stishovite and MgSiO<sub>3</sub> akimotoite samples were synthesized at high pressure and high temperature. The thermal Gruneisen parameters were obtained from weighted average of the mode-Gruneisen parameters which were determined from pressure shifts of Raman peaks. Thermal expansivities were calculated from the Gruneisen equation. The heat capacities at constant volume ( $C_V$ ) were calculated using lattice vibrational model. High-temperature X-ray diffraction measurements of MgSiO<sub>3</sub> akimotoite were performed in a temperature range of 293.8 - 773 K. The thermal expansivity was determined from the temperature dependence of the unit cell volume.

Obtained thermal expansivities were expressed using the polynomial of temperature:  $\alpha = a + bT + cT^{-1} + dT^{-2}$ . The coefficients for SiO<sub>2</sub> stishovite and MgSiO<sub>3</sub> akimotoite were determined to be  $a = 1.85E-5$ ,  $b = 3.25E-9$ ,  $c = -2.41E-3$ ,  $d = -1.11E-1$ , and  $a = 2.53E-5$ ,  $b = 7.62E-9$ ,  $c = -8.63E-4$ ,  $d = -5.51E-1$ , respectively.

The thermal expansivity of SiO<sub>2</sub> stishovite in this study is smaller than that obtained from high-pressure high-temperature in situ XRD measurements by Nishihara et al. (2005), and agrees with that obtained from optimization of thermodynamic data assessment by Mao et al. (2001). The heat capacity at constant pressure ( $C_P$ ) calculated using the thermal expansivity by Nishihara et al. (2005) is 5 % larger than that measured by thermal relaxation method by Akaogi et al. (2011). On the other hand,  $C_P$  calculated using the thermal expansivity of this study shows good agreement with Akaogi et al. (2011). Therefore, our thermal expansivity of stishovite is internally consistent with the measured heat capacity data.

Our thermal expansivity of MgSiO<sub>3</sub> akimotoite derived by the theoretical method is closer to those determined by high-temperature XRD measurements in this study and Ashida et al. (1988) rather than that of Wang et al. (2004) obtained from high-pressure high-temperature in situ XRD measurements. This result suggests that the thermal expansivity of MgSiO<sub>3</sub> akimotoite is larger than previously reported values.

Keywords: akimotoite, stishovite, thermal expansivities, high-pressure Raman spectroscopy, high-temperature X-ray diffraction measurements

## The synthetic opal fixed in hydrothermal environment

Yuko Yamasaki<sup>1\*</sup>, Hiroshi Isobe<sup>1</sup>

<sup>1</sup>Grad. Sch. Sci. Tech., Kumamoto Univ

Opal shows a characteristic opalescence by periodic stacking of amorphous silica spherules with several hundred nanometers in diameter. The amorphous silica spherules can be synthesized by the Stoeber method with hydrolysis of tetra ethyl orthosilicate (TEOS) solution. The initial silica spherules are dispersed in suspension. In this study, we report stable synthetic opal with opalescence domains fixed in hydrothermal conditions.

The silica spherule suspension made by the Stoeber method is concentrated and poured in silica glass test tube with 6mm in inner diameter and approximately 30mm in height. The silica test tubes are sealed in teflon crucibles or microreactors with distilled water and heated to 100 degrees Celsius - 250 degrees Celsius for 1 to 75 days. Depth of distilled water outside the silica glass test tubes does not exceed the height of the test tube. After the run durations, surface of the settled silica is covered with resin and cut to observe vertical section by optical and electron microscopes.

In the run products of 100 degree C to 200 degree C, we can see opalescence domains up to mm scale. Especially, in the run products of 200 degree C, we can see development of opalescence domains with various colors. Under the electron microscopy, deformation of silica spherules or cementation is observed in run products with opalescence. The hydrothermal environment can play essential role to form opalescence domains and fixation from amorphous silica spherule suspension.

Keywords: opal, hydrothermal synthesis, opalescence domain, amorphous silica

## Activation of hole charge carriers and generation of electromotive force in gabbro blocks induced by non-uniform loading

Akihiro Takeuchi<sup>1\*</sup>, Toshiyasu Nagao<sup>1</sup>

<sup>1</sup>Earthq. Predict. Res. Cent., Inst. Oceanic Res. Dev., Tokai Univ.

When one end of vacuum-dried gabbro blocks was subjected to uniaxial loading, the unloaded end became electronically positive (+80 mV at 50-MPa). Hot point probe tests using the hot-probe with 423 K of the temperature and the cold one with 293 K found that the Seebeck coefficient of the loaded volume decreased from  $\sim 15.8$  mV/K to  $\sim 14.9$  mV/K when loaded, while the coefficient of the unloaded end did not change remarkably ( $\sim 15.6$  mV/K). This means that this gabbro originally included a small number of hole charge carriers and the carriers in the loaded volume increased when loaded. From the viewpoint of the fundamental band model of solid state, the most reasonable mechanism of the increment is the decrease of the energy gap between the acceptors and the valence band top. Shear stress/strain would effectively shift the energy levels because early studies have found that the electronic conductivity of gabbro is almost independent of the hydrostatic pressure. Based on this idea, a generation model of the stress-induced electromotive force is proposed. Since this model is expected to be universally applicable to various types of rocks, similar electromotive forces in the crustal scale may be induced by seismic, volcanic, and tidal activities in the Earth and Moon.

Keywords: gabbro, hole charge carrier, electromotive force, Seebeck coefficient

## Ferrous to ferric ratio measurement in chlorite using electron energy-loss spectroscopy (EELS)

Sayako Inoue<sup>1\*</sup>, KASAMA, Takeshi<sup>2</sup>, Kogure, Toshihiro<sup>1</sup>

<sup>1</sup>Earth & Planetary Sci., Univ. Tokyo, <sup>2</sup>Center for Electron Nanoscopy, DTU

Determination of  $\text{Fe}^{3+}/\text{Fe}_{\text{total}}$  ratio in iron-bearing minerals is important and has been conducted using several analytical techniques such as Mosbauer spectroscopy, X-ray absorption near-edge structure (XANES) and X-ray photoelectron spectroscopy. Compared to these techniques, electron energy-loss spectroscopy (EELS) in Transmission electron microscopy (TEM) is capable of giving information of the chemical state of constituting elements in specimens, with a spatial resolution down to the nanometer scale. Detailed analysis of energy-loss near-edge structure (ELNES) of Fe-L<sub>2,3</sub> core-loss edges provides information about the iron oxidation state, and several methods have been proposed to quantify  $\text{Fe}^{3+}/\text{Fe}_{\text{total}}$  from the ELNES of iron (Garvie and Buseck, 1998; van Aken et al., 1998). However, because a number of silicate minerals are electron-beam sensitive, the influence of radiation damage on the quantification of  $\text{Fe}^{3+}/\text{Fe}_{\text{total}}$  by EELS should be considered. Moreover, sample preparation processes for TEM such as argon ion-milling and focused-ion-beam (FIB) milling form a damage layer on the specimen surface, which may also affect the quantification. In this study  $\text{Fe}^{3+}/\text{Fe}_{\text{total}}$  quantification in chlorite, rather beam-sensitive iron-bearing phyllosilicates, has been performed using EELS equipped to a field-emission gun TEM with a monochromator, considering the influence of radiation damage and sample conditions on the measurement.

$\text{Fe}^{3+}/\text{Fe}_{\text{total}}$  ratios obtained from the same grain of chlorite indicated that the ratio increases significantly with the electron dose to be radiated during TEM observation and EELS acquisition, suggesting that the oxidation of iron proceeds with vitrification of chlorite by radiation. Hence, it was necessary to acquire several  $\text{Fe}^{3+}/\text{Fe}_{\text{total}}$  ratios as a function of electron dose (i.e., time) and estimate 'the damage-free ratio' by extrapolation. The surface damage layers with a thickness of several tens of nanometers, which were formed during FIB milling, are likely oxidized and therefore partially associated with the increase in the  $\text{Fe}^{3+}/\text{Fe}_{\text{total}}$  ratios.

Keywords: EELS, TEM, Phyllosilicate, Chlorite, Iron valence state, FIB

## Change in fayalites with ultraviolet rays and water

Nobuo Komori<sup>1\*</sup>

<sup>1</sup>Ota ward Kamata junior high school

I have been doing an experimental research of weathering on rocks by ultraviolet rays and waters in a junior high school science club since 2002. This time, it aimed to see the reaction of fayalite when it is soaked in distilled water and irradiated with ultraviolet rays.

It is said that there is much basalt that perhaps contains fayalite on Mars surface. Moreover, it is estimated that there was water on Mars surface in the past. Therefore, I think that ultraviolet rays and water are one of the factors which change rocks on Mars surface.

In this research, fayalites, which total weight is about 10g, are put in the test tube filled with distilled water. The diameter of these fayalites is about 3mm~5mm. They are grain shaped and the color is dark green. The test tube is irradiated with ultraviolet rays with their peak wave length of 254 nm. Another experiment was done as a comparison under the same condition but without ultraviolet. The tubes were irradiated with ultraviolet rays for three months. The illuminance of ultraviolet rays is 40w/m<sup>2</sup> when the experiments were first started.

As a result of this experiment, a lot of light brown powder was generated in both of the test tubes that were irradiated with ultraviolet rays. However, the tube without ultraviolet rays irradiation generated less powder. Therefore, we can conclude that irradiation of ultraviolet rays causes larger amount of the powder. From the result of EPMA analysis, the powder is the amorphous iron oxide hydroxide.

There are many fresh structures that is like hole about 10micron m on uv irradiated fayalite.

But there are few these structures on uv not irradiated fayalite.

Moreover, we can estimate that ultraviolet rays might promote the change of fayalites in the water. It is presumed that water existed in the past on Mars surface.

I think that there is a possibility on the Mars surface that the rocks contained fayalites were oxidized by the water and ultraviolet rays.

Keywords: ultraviolet rays, water, fayalite, iron(III) oxide, change, Mars

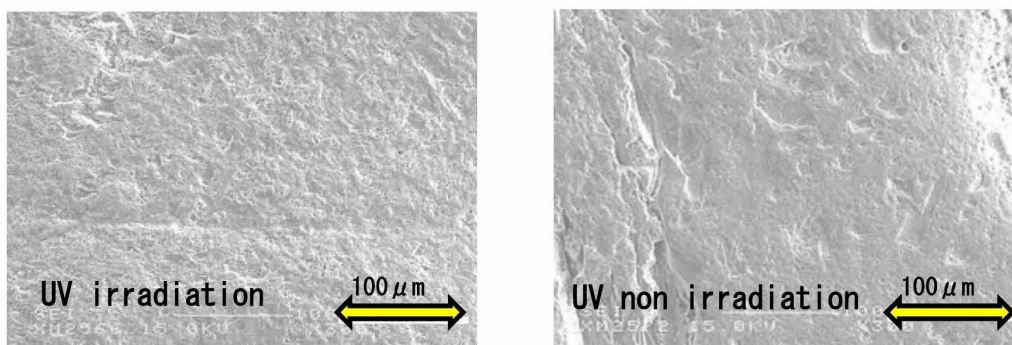


Fig. SEM images of the surfaces of fayalite specimens soaked in distilled water for 3 months with and without UV irradiation.

## Annealing and radiation effects on cathodoluminescence of zircon

Yuta Tsuchiya<sup>1\*</sup>, Masahiro Kayama<sup>2</sup>, Hirotsugu Nishido<sup>1</sup>, Yousuke Noumi<sup>1</sup>

<sup>1</sup>Department of Biosphere-Geosphere Science, <sup>2</sup>Department of Earth and Planetary Systems Science

Cathodoluminescence (CL) analysis provides useful information on the existence and distribution of defects and trace elements in materials, which are related to genetic conditions such as formation temperature, metamorphic process and geochronological situation. U-Pb zircon dating (e.g., SHRIMP) is an important tool to determine geological age of a micro-ordered zircon, where CL image has been used for observation of internal zones and domains with different chemical compositions and structural disorder at spatial high resolution. CL of zircon is caused by various types of emission centers, which are divided into two groups: extrinsic center such as rare earth element (REE) and intrinsic center such as lattice defects. Above all, CL of zircon is closely related to metamorphic process and radiation from contained radionuclides. Most zircon has yellow emission, which seems to be assigned to radiation-induced defect or UO<sub>2</sub> centers. According to Nasdala et al. (2002) and Hancher and Hoskin (2003), the yellow emission band has been recognized to be eliminated by heat treatment. Therefore, the radiation effects on zircon CL have been studied for He<sup>+</sup> ion-implanted samples annealed at various temperatures to clarify radiation-induced defect centers involved with yellow CL emission in zircon.

A single crystal of zircon from Malawi (MZ) was selected for annealing and He<sup>+</sup> ion implantation experiments. The sliced samples were cut perpendicular to c- and a- axes, and annealed at 100 to 1400 deg. C for 12 hours. Zircon crystals in Takidani granodiorite (TZ) and Kurobegawa granite (KZ), and the sliced MZ were implanted by He<sup>+</sup> ion at 4.0 MeV corresponding to energy of alpha particle from <sup>238</sup>U and <sup>232</sup>Th. The radiation dose was set at 4.77 x 10<sup>-4</sup> and 5.11 x 10<sup>-5</sup> C/cm<sup>2</sup>. CL spectra in the range from 300 to 800 nm with 1 nm step were measured by a scanning electron microscopy-cathodoluminescence (SEM-CL). The operating condition was set at 15 kV accelerating voltage and 0.1 nA beam current. All CL spectra were corrected for the total instrumental response.

CL spectra of untreated and annealed zircon almost show emission bands at ~370 nm assigned to intrinsic defect center and at ~480, ~580 and ~760 nm to Dy<sup>3+</sup> impurity centers [Cesbron et al, 1995; Gaft et al, 2005]. Yellow CL emissions have been undetected in annealing zircons above 700 deg. C, where an elimination of radiation-induced defect centers may be appeared due to recrystallization of the structure suggested by Nasdala et al (2002). Blue CL intensity at ~370 nm gradually increases with an increase in annealing temperature, which may be responsible for a formation of intrinsic defect center due to a recovery of the framework structure from metamict by heating. CL spectra of MZ show an increase in the yellow emission intensity with an increase in radiation dose of He<sup>+</sup> ion implantation as well as the emission related to the impurity centers (REE), though He<sup>+</sup> ion implantation reduces the intensity of impurity centers. Yellow emission intensity has a tendency to depend on radiation dose of He<sup>+</sup> ion implantation. TZ and KZ, with young formation ages of 1.93-1.20 Ma and 1.7-0.9 Ma, respectively [Harayama,1994; Harayama et al., 2010], show dull yellow CL emission attributed to radiation-induced defect center, suggesting relatively low radiation dose of alpha radiation from <sup>238</sup>U and <sup>232</sup>Th on them. If the component of yellow emission could be deconvoluted from the CL spectra in zircon, the intensity of yellow emission should be used for an indicator to evaluate total exposure doses on it during geological age.

Keywords: Cathodoluminescence, Zircon, annealing effect, radiation effect

## Emission mechanism of cathodoluminescence in smithsonite

Masato Makio<sup>1\*</sup>, Hirotsugu Nishido<sup>1</sup>, Nobuhiro Kusano<sup>1</sup>, Kiyotaka Ninagawa<sup>1</sup>

<sup>1</sup>Okayama Univ. Sci.

Cathodoluminescence (CL) has been widely applied in mineralogical investigation, especially for carbonates. CL of carbonates is characterized by various types of emission centers such as impurity and defect centers. Smithsonite ( $\text{ZnCO}_3$ ) has emission centers of divalent Mn ion as activator and divalent Fe ion as quencher (Gotte and Richter, 2004). However, the defect center in smithsonite has not been investigated so far, since its emission is not so often found in carbonates. We have detected blue CL emission in smithsonite, suggesting structural defect center. In this study, we have assigned emission bands in CL spectra including defect center and clarified the mechanism of the CL in smithsonite in a wide temperature range.

Three crystals of smithsonite from San Antonio, Mexico (S-08, S-11) and Slaiman, Uzbekistan (S-17) were selected for CL measurements after carbon-coating on their polished surfaces. SEM-CL analysis was conducted using an SEM (JEOL: JSM-5410) combined with a grating monochromator (Oxford: Mono CL2) to measure CL spectra ranging from 300 to 800 nm in 1 nm steps at accelerating voltage of 15 kV and beam current of 1.0 nA. The CL emitted from the samples was collected by a photon counting method with a photomultiplier tube, and converted to digital data. All spectra were corrected for total instrumental response determined using a calibrated standard lamp. The sample temperature can be controlled in the range from -190 to 50 degree C with flowing liquid nitrogen and using an embedded heater in a cryostage (Oxford: C1003). CL color imaging was carried out with Luminoscope (ELM-3 R) consisting a cooled CCD camera by excitation voltage at 10kV and beam current of 0.5 mA.

CL spectra of S-11 at room temperature show a broad band at around 650 nm in red region, which can be assigned to the electronic transition from excited state of 4G to ground state of 6S corresponding to divalent Mn activator substituted for Zn ion. S-08 has a broad band at around 400 nm in blue region in its CL spectrum. Its emission might be caused by the defect center in smithsonite lattice. S-17 has also emission peaks at around 650nm in red region and 400nm in blue region. The deconvolution of the spectra in an energy unit using a Gaussian fit reveals that a red emission has two components peaked at 1.61 and 1.82 eV and a blue emission consists of two components at 3.28 and 3.82 eV. Therefore, there are at least two different defect centers in smithsonite, suggesting different crystal fields between them. The intensity of a blue emission decreases with an increase of sample temperature as explained by a temperature quenching theory based on an increase in the probability of non-radiative transition with the rise of temperature (Mott-Seitz model). Activation energy in each temperature quenching process can be calculated by an Arrhenius plot using integrated intensity of each component as a luminescent efficiency. It results in activation energy of 0.027 eV for component centered at 3.28 eV. This energy value corresponds to the energy of O-Zn-O bending vibration (0.024 eV: Frost et al, 2008), suggesting energy-transfer from the radiation to lattice vibration as phonon. However, the intensity of a red emission is not affected by the change of sample temperature. These facts indicate that the temperature quenching mechanism might depend on the types of emission centers related to impurity or structural defect.

Keywords: smithsonite, cathodoluminescence, emission mechanism

## Numerical definition of particle size and shape of volcanic ash by statistical particle image analysis method.

Daisuke Sasakura<sup>1\*</sup>, HAYAUCHI Aiko<sup>1</sup>

<sup>1</sup>Malvern Japan ,Div of Spectris Co.Ltd.,

### [1] Introduction

The exact definition of particle size and shape is a factor of importance in many researches connected with several geology sciences which objections are sea sand, soil and volcanic ash. The object of this report is to describe the various methods of defining these properties and to give the result of some measurements made on volcanic ash as model sample by statistical particle image analysis.

### [2] Methodology

The statistical particle image analysis is possible to obtain the significant difference evaluated result of particle size and shape information by over the ten thousand numbers of particles projection images from microscopic method. The methodology of this technique is based on the digital binary image processing technology from projection image picture of CCD camera on microscope. In each CCD camera pixels has size. The determinations of particle size and shape parameter are calculated by the particle projection images which are constructed from the number pixels in CCD camera. The most of the advantage of this method is not only possible to described numerical definition of particle analysis but also available to the diverse analysis by two dimensional correlations plot between shape parameter and particle size.

### [3] Material and method

Volcanic ash sample was from the Ito Pyroclastic Flow as model sample. This sample was sieved by 5 phi mesh sieve and it was come from under the mesh to isolate small particle from bulk sample. An automated particle characterization system (Morphologi G3, Malvern Instruments) was used to evaluation of statistical particle image analysis. The observation mode was diascopic mode (Transmittance mode) . Volcanic ash sample were dry dispersed using the integrated Dry sample dispersion unit via an instantaneous pulse of compressed air, and measured using Standard Operating Procedures (SOPs) which define the software and hardware settings depending. Measurements were made in an enclosed glass plate as sample carrier, minimizing environmental exposure. The analysis generated high quality images from over ten thousands of sample particles.

### [4] Result

Total number of 96,029 particles was measured. Volume based circle equivalent diameter of particle size distribution (VCED) were monomodal and 14.31(d10), 30.32(d50), 45.79(d90) in micro meter. However, the number based percentage of small particles (<3 micrometer) was 74.91%. To concerning shape distribution and shown in Fig.1. Circularity was bimodal, however aspect ratio was monomodal. Recalculation of VCED was shown Fig.2 which was shape distribution data. Represented on amount of volume based percentage , the circle like particles were 3% and the angular like particles were 64% .However , in count based percentage , circle like particles were 55% and angular like particles were 21%.

### [5] Summary

This report will be more discuss about application and capability of numerical definition of volcanic ash by the statistical particle image analysis as new approach for this research area.

Keywords: Volcanic Ash, Particle size, Particle shape, Particle Image Analysis

SMP44-P12

Room:Convention Hall

Time:May 20 18:15-19:30

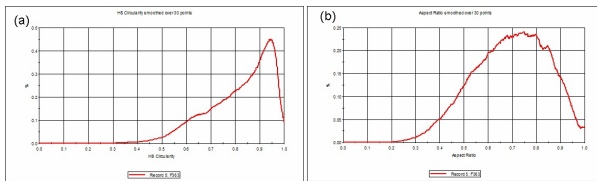


Fig.1 Shape distribution by particle image (a) Circularity (b) Aspect ratio

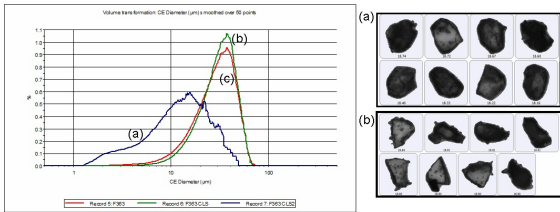


Fig.2 Recalculated VCED (a) Circle like (Circularity  $\geq 0.850$  Aspect Ratio  $\geq 0.450$ ) (b) Angular like (Circularity Between 0.400 - 0.750 , Aspect Ratio  $\geq 0.450$ ) (c) Total

## Temperature quenching mechanism of cathodoluminescence in dolomite

Nobuhiro Kusano<sup>1\*</sup>, Hirotsugu Nishido<sup>1</sup>, Masato Makio<sup>1</sup>, Kiyotaka Ninagawa<sup>1</sup>

<sup>1</sup>Okayama University of Science

Cathodoluminescence (CL) has been widely applied in mineralogical and petrological investigations, especially for carbonates. Dolomite commonly red CL emission related to an impurity center of divalent Mn (Reeder, 1987; Gillhaus et al, 2001), but of which each occupancy in Ca site (A site) and/or Mg site (B site) has not been precisely estimated. Furthermore, temperature effect on CL efficiency has not been discussed in spite of potentially important function to control CL emission mechanism, though the factors effected on dolomite CL such as luminescence centers have been extensively investigated. In this study we have clarified luminescent mechanism of dolomite in a wide range of temperature using a SEM-CL, and confirmed a temperature quenching of its emissions. The quenching process has been quantitatively evaluated by CL spectral deconvolution method assuming the Mott-Seitz model, where site occupancy for Mn<sup>2+</sup> ions in dolomite lattice has been also evaluated.

Three dolomite samples from Binntal/VS, Swiss (D-17a), Arizona, USA (D-26a) and New Mexico, USA (D-28a) were selected for CL measurements after carbon-coating on their polished surfaces. These samples contain Mn<sup>2+</sup> ions as an activator, but too low for divalent Fe as a quencher.

SEM-CL analysis was conducted using an SEM (JEOL:JSM-5410) combined with a grating monochromator (Oxford: Mono CL2) to measure CL spectra ranging from 300 to 800 nm in 1 nm steps with a temperature controlled stage from -190 to 250 °C. The dispersed CL was collected by a photon counting method using a photomultiplier tube (R2228) and converted to digital data. All CL spectra were corrected for the total instrumental response.

All samples exhibit a broad band in red region CL spectrum between 580 and 640 nm at room temperature. The spectral peaks are sharpened and enhanced at lower temperature due to reduction of thermal lattice vibration and an increase in luminescent efficiency, suggesting high spectral resolution of the emission bands at low temperature. Therefore, a Gaussian fitting was conducted to quantitatively deconvolute spectral data obtained at low temperature in an energy unit. Two emission components at around 1.84 and 2.15 eV. The former can be assigned to the emission derived from Mn ion impurity occupied at A site, the latter to the emission at B site. The component intensities decrease in two steps of temperature range between -190 to -100 and -50 to 150 °C with an increase in sample temperature. In general, luminescence efficiency of the material decreases with a rise in temperature due to an increase in non-radiative transitions. This phenomenon has been recognized in several minerals such as quartz, cristobalite and tridymite as temperature quenching. By assuming the Mott-Seitz model, activation energy in temperature quenching process can be calculated by a Arrhenius plot using integrated intensity of each component as an emission efficiency. Each activation energy was determined as follows; 0.03 eV for A and B sites below -100 °C and 0.100 eV for A site and 0.097 eV for B site above -50 °C. The former corresponds to the value of CO<sub>3</sub> vibration, and the latter to Ca-O or Mg-O vibration. Judging from the similarity of the activation energy in the process of temperature quenching and lattice vibration energy, the temperature quenching energy might be transferred as a phonon to the specific lattice vibration through non-radiative transition.

Keywords: dolomite, cathodoluminescence, temperature quenching